Dynamics of a helical swimmer crossing an interface between two immiscible fluids

Jorge Gonzalez-Gutierrez,[1,2] Salvador Osorio-Ramirez,[2]
Francisco J. Solorio-Ordaz,[1] and Roberto Zenit[2,*]
[1]*Departamento de Termofuidos, Facultad de Ingeniería, Universidad Nacional Autónoma de México, Avenida Universidad 3000, Mexico, D.F., 04510, Mexico*
[2]*Instituto de Investigaciones en Materiales, Universidad Nacional Autónoma de México, Avenida Universidad 3000, Mexico, D.F., 04510, Mexico*

(Received 22 February 2019; published 9 August 2019)

In this study, we experimentally investigate the mechanical process of a self-propelled helical swimmer to move across an interface between two immiscible fluids. This configuration is aimed to emulate some aspects of the process used by bacteria to trespass mucus layers or epithelial cell membranes to cause infections. We consider two configurations: head-first and tail-first. We find that, in both cases, the head of the swimmer deforms the interface generating a meniscus that induces a significant reduction of the swimming speed, that lasts until the interface is pierced. In both cases, the dynamics of penetration is complex leading to significant variations of the swimming speed during the process. We observed interesting differences in the penetration dynamics for the two cases; we argue that the differences arise from the significantly different shape and direction of the menisci that forms during the penetration process. A model that accounts for thrust, drag, buoyant, and capillary forces is used to rationalize the results.

DOI: 10.1103/PhysRevFluids.4.083102

I. INTRODUCTION

Migration of microorganisms and cells in higher organisms play a critical role in sexual reproduction, the performance of chemical reactions, and providing essential nutrients [1,2]. The locomotion process of such microorganisms commonly occurs through a complex environment composed of potentially hostile immune cells, non-Newtonian liquids, and highly viscous regions where the inertial forces are negligible [3]. In simple words, self-propulsion is a crucial mechanism for microbiological survival.

In the human body, many motile bacteria have multiple functions, affecting the organism positively or negatively, according to their nature [4,5]. For example, many bacteria serve as an auxiliary participant in digestion through the fermentation of some foods, the activation of yeast, etc. They can also act to influence brain receptors that identify the taste of food [6,7]. More importantly, many microorganisms cause health disorders by infections. The first step toward an infection is the migration of such microorganisms. Some tissues are vulnerable to infections, such as eyes, nasal passages, respiratory tract, mouth, digestive tract, urinary tract, and female genital tract. The vulnerability results from the fact that such tissues are exposed to the environment, such that oxygen and nutrients are easily absorbed. Naturally, such exposed tissues possess different strategies to cope with the penetration of harmful microorganisms. However, sometimes the protection fails and bacteria do cross the epithelial barriers. For example, anaerobic bacteria of the genus *Bacteroides*,

*Corresponding author: zenit@unam.mx

usually found the intestinal flora, can induce lethal peritonitis if they enter the peritoneal cavity through a wound in the intestines [8,9]. More interesting is the case when the microorganisms actively attempt to penetrate the natural barrier to infect a host. A fascinating example is that of *Helicobacter pylori*, which causes ulcers by penetrating the gastric mucous [10,11]. These bacteria are the only ones capable of colonizing the highly acidic environment of the human stomach. They are capable of surviving and thriving in this environment by producing urease, which, by catalyzing the hydrolysis of urea, produces ammonia, which elevates the pH of its close vicinity. *H. pylori* is capable of infecting its host by swimming across the gastric mucous to reach the stomach wall. The process through which this is achieved is poorly understood.

The intestinal mucous is composed of an inner layer lacking in bacteria and an outer layer that serves as a habitat for commensal bacteria. The pathogenesis of *H. pylori* infection, which could lead to severe inflammation and even result in the onset of cancer, begins with the penetration of the inner layer of the gastric mucus. It has been reported that this process is possible thanks to the motility of the battery mediated by its flagella and the enzymatic degradation between the two layers [12]. The motion of *H. pylori* across the gastric mucous barrier occurs due to a rupture of symmetry by the helical motion [12]. Its locomotion is achieved by rotation of flagella, which are slender helical appendages, whose capability to rotate produce propulsive forces to push the microorganisms forward [13].

The process of bacteria crossing an interface may also be relevant for environmental remediation. Hydrocarbons degradation by bacteria is a complex process where many direct and indirect interactions occur among different factors of a complex ecological network that coexist around oil droplets [14–16]. During this process, bacteria have the capacity to exploit hydrocarbons as a source of energy thanks to their metabolic capacity. Some bacteria, such as *Alcanivorax borkumensis*, are located at the aerobic, alkane-rich areas of shorelines and the oxygen-rich layers of the oil droplets [14]. Although it is believed that the digestion process takes place at the surface of the drops, some partial penetration is expected. In general, bacteria need to actually pierce the droplet interface to initiate the digestion process of hydrocarbons [15,16].

The motility of these microorganisms through a fluid environment is driven by several physicochemical processes that lead to nonlinear elasticity, screened electrostatics, interactions with diffusing chemicals, and biochemical noise [17]. In all cases, the flagellar dynamics occur in a low-Reynolds environment. Hence, the hydrodynamics are dictated by the prevalence of viscous forces and the absence of inertia. For bacteria the Reynolds number, Re, typically ranges from 10^{-4} to 10^{-2}. For such a regime, it is possible to obtain analytic solutions and predicts the swimming speed of simplified geometries [18]. The formulation of the classical resistive-force theory for swimming is a good example of the advantages of this regime [19,20].

The use of artificial swimmers, as opposed to actual organisms, has been instrumental to improve the understanding of bacterial locomotion. Swimmers that retain the fundamental aspects that lead to locomotion in low Re environments can be manipulated and modified to perform controlled displacements from which many detailed aspects of swimming can be studied, particularly in complex environments. An example of the development of artificial swimmers is the magnetically driven helices of Zhang *et al.* [21]. Consisting of a magnetic head, attached to a helical tail, the swimmers propelled themselves by rotation their head under the action of an external magnetic field. This simple arrangement emulated the swimming strategy of bacteria like *Escherichia coli* [22].

Although for the case of bacteria or artificial swimmers, the dynamics of crossing an interface or a membrane have hardly been studied, there is a vast literature about the motion of objects moving through interfaces [23–29]. Such a configuration is of significant importance for many practical applications. Many investigations have addressed the case of a rigid particle crossing through a two-layer interface of immiscible Newtonian fluids, settling or ascending by their own weight or buoyancy. This flow exhibits a variety of patterns depending on the values of the relevant dimensionless parameters such as the interfacial Bond number and the Archimedes number. These dimensionless groups are appropriate to study the gravitational motion of objects. When the inertial effects dominate over surface tension ones (large Bond number), as in the case when a sphere

TABLE I. Properties of test fluids. The fluids used for the mixtures were purified water (W), glucose (G, Karo corn syrup) and two silicone oils (S1, DMS-T23 and S2, DMS-T43 from Gelest Inc).

Fluid	Composition % vol	Density, ρ kg/m^3	Viscosity, μ Pa s
S1/S2 mixture	20/80	900	2.3
W/G mixture	10/90	1200	2.3

impacts a water-air interface, a splash is formed characterized by the generation of a circular crown of ligaments and droplets. Moreover, it possible to observe the development of an air cavity that connects the free surface and the sphere [30,31]. In the opposite limit, when the speed is small due to a small density difference, no splash occurs. For this case, two basic configurations have been identified [24,25]. For the first one, the "film drainage" regime, the sphere crosses the interface entirely only after the liquid film that forms ahead of it has been drained completely. In general, this process is the slowest step during the penetration of the interface [32,33].

For the so-called "tailing" regime, a sphere penetrating an interface drags a column of one fluid into the other. This entrained fluid volume eventually pinches off, and a part of the fluid column recedes toward the initial position of the interface while the other part may remain attached to the particle. The tail dynamics generally differs from that of a cavity due to the vorticity levels in the first one makes the flow field entirely different from a potential flow [24,34,35]. In this context, there are some studies focused on quantitative observations of the film drainage, tailing configurations, interface deformation, and induced velocity field that emerge during the penetration dynamics of millimeter-size spheres in a fluid-fluid interface [36–40]. As shown below, the penetration dynamics of helical swimmers share some resemblance with the tailing regime.

In this paper, we report an experimental study of the dynamics of helical magnetic robots, displacing either *head-forward* or *tail-forward*, crossing through the interface between two immiscible fluids. We find that the crossing process is different for the two configurations but share some common features. For both cases, the head deforms the interface forming a meniscus that slows the swimming speed significantly; conversely, the helical tail deforms the interface with the reverse curvature causing the surface tension force to enhance the swimming speed. The study aims to provide some understanding of this interfacial penetration process from a mechanical point of view, which may be relevant to understand how bacteria produce infections.

II. EXPERIMENTAL SETUP AND MATERIALS

To study the dynamics of the penetration process of a low-Reynolds number swimmer across the interface of two immiscible fluids the following experimental device was designed and built. We used the helical swimmer previously used by our group to study swimming in complex media [41,42]. The swimmer propels itself by the rotation of a rigid helix that is attached to the head. The head, which contains a small permanent magnet, is rotated by the action of an external magnetic field [43]. With this configuration, the swimmer displaces itself without an imposed external force.

A square acrylic container of $7 \times 7 \times 18$ cm^3 was filled with two immiscible liquids (equal volume each), which had slightly different densities but the same viscosities. The properties of these liquids are shown in Table I. Both liquids were mixed slowly and left still for at least 24 h, such that bubbles would not be present. First, the heavy liquid (a water-glucose mixture) was prepared; after its viscosity was determined, the second liquid was prepared by slowly adjusting the proportion of the two silicone oils to match, as close as possible, their values of viscosity.

The density of the fluid was measured with a 25-ml pichnometer. The fluid viscosity was measured with a viscometer (DV-III, Brokefield). The interfacial tension between the two fluids was not measured. A value of $\sigma_I = 0.05\,\mathrm{N/m}$ was inferred using the well-known Antonoff's formula, considering tabulated values of the surface tension for water and silicone oil ($\sigma_W = 0.07\,\mathrm{N/m}$ [44] and $\sigma_S = 0.02\,\mathrm{N/m}$, from the technical data from the manufacturer, Gelest Inc).

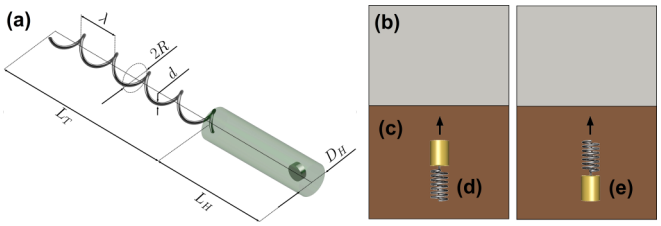

FIG. 1. The experimental setup. (a) The helical swimmer. The dimensions of the device are: $D_h = 3$ mm; $L_h = 16$ mm; $L_t = 16$ mm; $\lambda = 5.3$ mm; $2R = 3$ mm; and the pitch angle $\theta = 45^\circ$. The thickness of the wire, d, was 0.9 mm. (b) The upper and (c) the lower fluids. The swimmer with (d) head and (e) tail firsts.

The swimmer, depicted schematically in Fig. 1(a), was placed inside the container, initially in the lower fluid fixed by a release mechanism. The rotating magnetic coil and swimmer were arranged to make the robot swim in the vertical direction, moving perpendicularly to the interface between the two fluids, see Figs. 1(d) and 1(e). The average density of the swimmer was 1050 kg/m^3, slightly above the light fluid but slightly below the heavy fluid. Note that the density of the swimmer is not uniform, since the tail is denser than the head. Although their weights were similar (the head and tail weights were 0.172 and 0.175 g, respectively). The dimensions of the swimmer are reported in the caption of Fig. 1.

The motion of the swimmer and the penetration process were recorded with a high-resolution video camera (920 × 1080 pixels, Sony RX10II) at 60 frames per second. The position of the swimmer in time was obtained using the software Tracker. The swimming speed, U, was calculated using a central difference scheme. In all cases, the rotation speed of the swimmer was the same as that of the external magnetic field: in other words, the swimmer was operated below the step-out frequency of the arrangement [43].

Only one swimmer design was considered but a range of rotating frequencies were tested from 1.6 to 5 Hz; these frequencies lead to swimming speeds ranging from 4.22 to 6.34 mm/s in the lower fluid (U_o) and from 0.2 to 1.65 mm/s in the upper fluid (U_1), as shown in Fig. 2. The difference of swimming speeds for the two fluids, that have the same nominal viscosity, results from the fact that the density between the swimmer and the fluids is not matched: there is a small settling/rising speed for a non-rotating swimmer. For the heavy and light fluid, the terminal speed was $U_{b0} = 1.83$ mm/s and $U_{b1} = -1.29$ mm/s, respectively. The density mismatch simply adds an additional

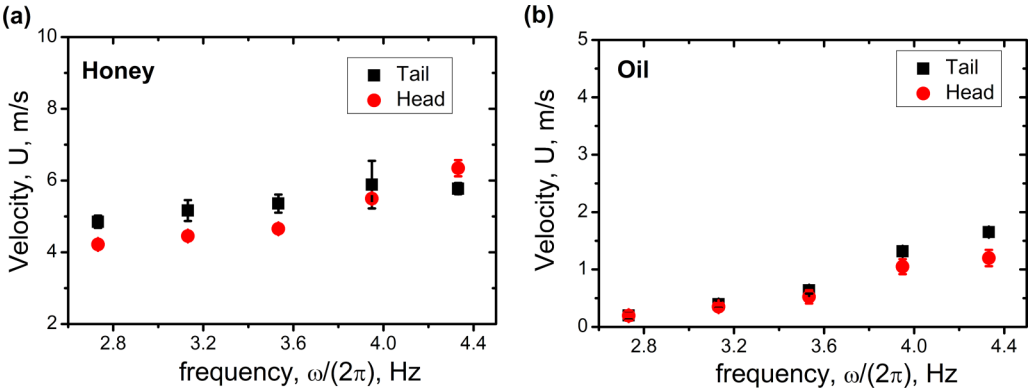

FIG. 2. The helical swimmer velocity without interface in (a) dense fluid, U_o and (b) light fluid, U_1. The physical properties of the fluids are shown in Table I. The error bars indicate the measurement uncertainty.

force (effective weight) that is accounted for in our analysis. Note that for all frequencies $U_o \approx U_1 + (U_{bo} - U_{b1})$.

To characterize the motion of the swimmer through the interface, we consider two dimensionless groups: the Reynolds and capillary numbers. The Reynolds number is defined as

$$\mathrm{Re} = \frac{\rho U_o D_H}{\mu}. \tag{1}$$

The value of Re had a maximum value of 0.01 for the entire experimental campaign. The capillary number, Ca, is defined as

$$\mathrm{Ca} = \frac{U_o \mu}{\sigma_I}. \tag{2}$$

For the range of speeds and liquid properties tested in this study, the capillary number spans from 0.184 to 0.288. It is important to emphasize that this set of dimensionless numbers is equivalent to that used for the case of settling spheres through interfaces (Bond and Archimedes numbers, Bo and Ar). From their definitions and considering that the characteristic gravitational velocity is $U_g \sim \sqrt{gD}$, we can show that $\mathrm{Re} = \sqrt{\mathrm{Ar}}$ and $\mathrm{Ca} = \mathrm{Bo}/\sqrt{\mathrm{Ar}}$. From the ranges in Bo and Re considered in this study, the crossing process of our swimmers resembles the tailing regime reported by Refs. [38,39].

For the biological case, Re is small as discussed above. For the capillary number, the properties of the cell membrane can be considered. In particular, the cortical tension (the equivalent of surface tension for membranes) can be as low as $10\,\mathrm{pN}/\mu\mathrm{m}$ [45]. Therefore, for a bacterial swimming ranging from 20 to $200\,\mu\mathrm{m/s}$ in water [46], the capillary number would range from $\mathrm{O}(10^{-3})$ to $\mathrm{O}(10^{-2})$. Considering the case when, instead of a membrane, the penetration takes place across a mucus layer, we can argue that the effective surface tension of such layer would be $\sigma \sim \mu_{\mathrm{layer}} U_o$ where μ_{layer} is the viscosity of the layer. Hence, the capillary number would be $\mathrm{Ca} \sim \mu/\mu_{\mathrm{layer}}$. For instance, the intestinal mucosal barrier has a viscosity similar to agarose gel [47], which ranges from 0.1 to 1 Pa s [48]. Therefore, the equivalent Ca for a mucus layer would also range from $\mathrm{O}(10^{-3})$ to $\mathrm{O}(10^{-2})$. Clearly, our experiments would not be directly comparable with the biological case but in both cases the surface tension effect is dominant.

We argue that a helical bacterium capable of crossing a mucous barrier would present a complex dynamic similar to that reported in this work, where abrupt changes in velocity depend strongly on the competition among the drag, thrust, buoyancy and interfacial tension forces. In this investigation, two swimming configurations are addressed. We found that the process of interface penetration was significantly different if the swimmer went head-first or tail-first. Hence, we conduct experiments in both situations, maintaining the rest of parameters fixed.

III. RESULTS

A. Head-first interaction

The first set of experiments consist in aligning the swimmer such that it swims directly toward the interface from the bottom of the tank but with its head first. In this manner, the process is mediated by the initial interaction of the head with the interface.

Figure 3 shows images of the process at different instants during the interaction with the interface. The complete dynamic of the helical swimmer is shown in Movie V1 (see Supplemental Material [49]). Along with the images, Fig. 4 shows the velocity of the swimmer as a function of position from the interface, indicating the same moments shown in Fig. 3.

The swimmer is initially held fixed at the bottom of the tank; when the rotating magnetic field is energized, to make it rotate, it is released and begins to move vertically at a constant speed, U. As the swimmer approaches the interface, its velocity progressively decreases, Fig. 3(a). The interface progressively deforms as the head reaches it, Fig. 3(b). The interface becomes largely deformed surrounding the head, Fig. 3(c); during this instant, the speed of the swimmer reaches a minimum

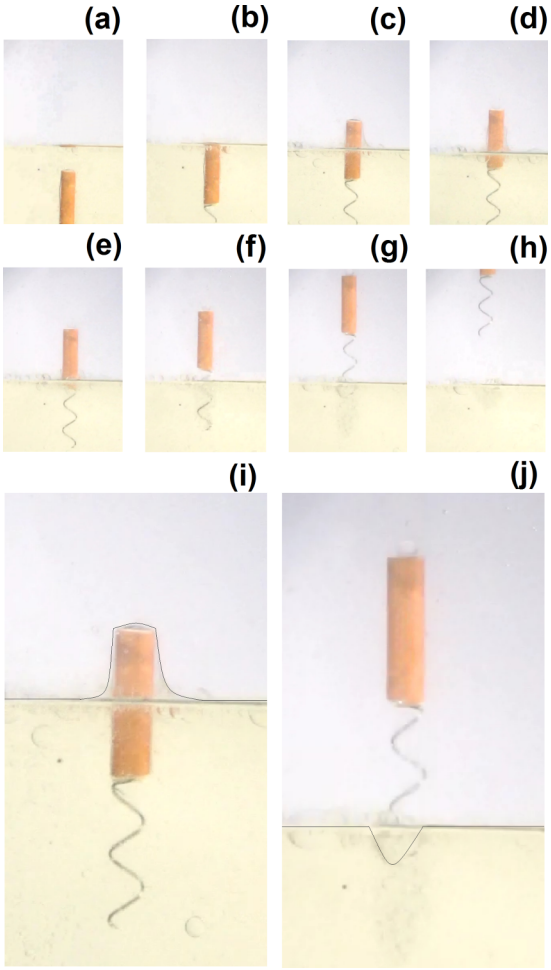

FIG. 3. Time sequence of the swimmer crossing the interface. (a)–(h) depict different relevant instants of the process, described in the text; these instants are also shown in the plot in Fig. 4. Images (i) and (j) show close-ups of the swimmer during the formation of the upper and the lower meniscus, respectively. A thin line was drawn at the interface location for clarity. The swimming speed for this case was 6.34 mm/s, which corresponds to a $\mathrm{Re} = 9.9 \times 10^{-3}$ and $\mathrm{Ca} = 0.29$.

value, $U_{\min}$. When the interface is finally pierced, Fig. 3(d), the swimmer increases its velocity as the head continues to cross the interface to reach a velocity U_p. When the head completes its passage through the interface, the speed decreases slightly, Fig. 3(e), as the meniscus retreats back. As the process progresses, the swimmer continues to move forward: the head is in the top fluid, but the tail remains in the lower fluid, Fig. 3(f). When the tail interacts with the interface, Fig. 3(g), the swimmer speed reaches a local maximum value, $U_{\max}$; during this time an "inversed" meniscus can be observed (into the lower fluid). Once the tail completely passes through the interface, the velocity gradually decreases, Fig. 3(h), reaching its new terminal value as it moves away from the interface. The process is also shown in terms of the swimming speed as a function of the head-position in Fig. 4. The dynamic of the meniscus can be observed in Movie M1 (see Supplemental Material [49]).

For all speeds tested, the behavior was similar. In Fig. 4, a second experiment conducted at a smaller speed is shown. The same features are observed in both cases; the magnitude of the characteristic speeds, $U_{\min}$, $U_{\max}$, U_p, do change.

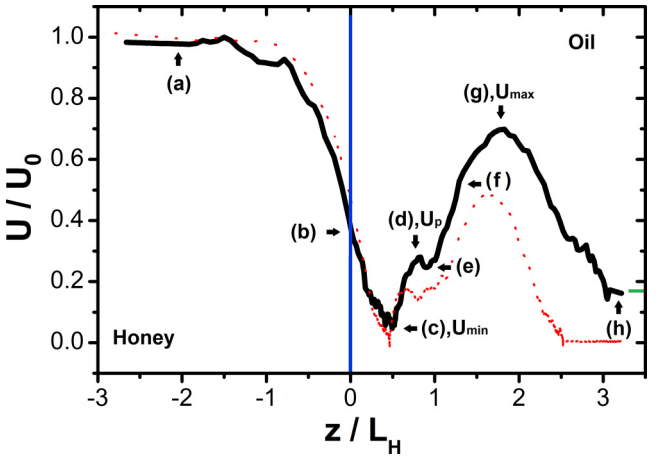

FIG. 4. Normalized speed of the swimmer U/U_o as a function of position, z/D_h. U_o is the speed of the swimmer in lower fluid without interface. The blue line indicates the location of the interface. The letters correspond to the time instants depicted in Fig. 3. The black-continuous and red-dashed curves correspond to swimmer speeds $U_o = 6.34\,\mathrm{mm/s}$ and $U_o = 4.22\,\mathrm{mm/s}$, respectively. The green line (lower right side) indicates the dimensionless swimming speed in oil (single phase).

The rich dynamics observed in Fig. 4 result from the intricate competition among the drag, thrust, buoyancy, and interfacial tension forces that emerge during the crossing process. The speed of the swimmer is modified during the crossing process resulting from two effects: the buoyancy forces and the interfacial tension forces. First, since the two-fluid arrangement is naturally stratified (the lower fluid is denser than the upper one), when the swimmer displaces from bottom to top, the buoyancy force changes from being in the direction of motion to be against it. Therefore, swimming speeds are different. Figure 2 shows that the speed of the swimmer is larger in the bottom fluid than in the top fluid, although the two fluids have the same viscosity. If the interface did not exert any other force over the swimmer, then the speed of the swimmer would gradually change from its value in the lower fluid to that in the top fluid. Hence, the speed of the swimmer is modified from the action of the interfacial force.

There are several instants during the penetration process that reveal the rich dynamics of the process. Figure 5 shows the value of the speed in three characteristic instants of the process, normalized by the initial speed. Since the dynamics of the process depends on the relative importance of the interfacial tension, the normalized speeds are shown as a function of the capillary number, Ca. The slowest speed during the penetration process, $U_{\min}$, occurs during the formation of a meniscus with large curvature, right before the interface is pierced. This instant is shown in Fig. 3(i). Figure 5(a) shows that $U_{\min}/U_o$ increases with Ca. Interestingly, for values smaller than $\mathrm{Ca} \approx 0.18$ the swimmer can no longer pierce the interface; it remains spinning at the interface, but it is not capable of pushing through. Figure 5(b) shows that once the swimmer is capable of piercing the interface, its velocity reaches a local maximum, U_{imp}, which also increases with Ca. Subsequently, when the tail interacts with the interface, a large meniscus with the opposite curvature (in comparison to when the head is passing through the interface) is formed. During this period the velocity reaches its maximum value during the crossing process $U_{\max}$. The normalized value of $U_{\max}/U_o$ also increases with Ca, as shown in Fig. 5(c). The images in Figs. 3(i) and 3(j) are close up of the instants in which the minimum and maximum speeds are observed. In these instants the interface deformation significantly affects the motion of the swimmer. This process will be discussed in detail in Sec. IV A, below.

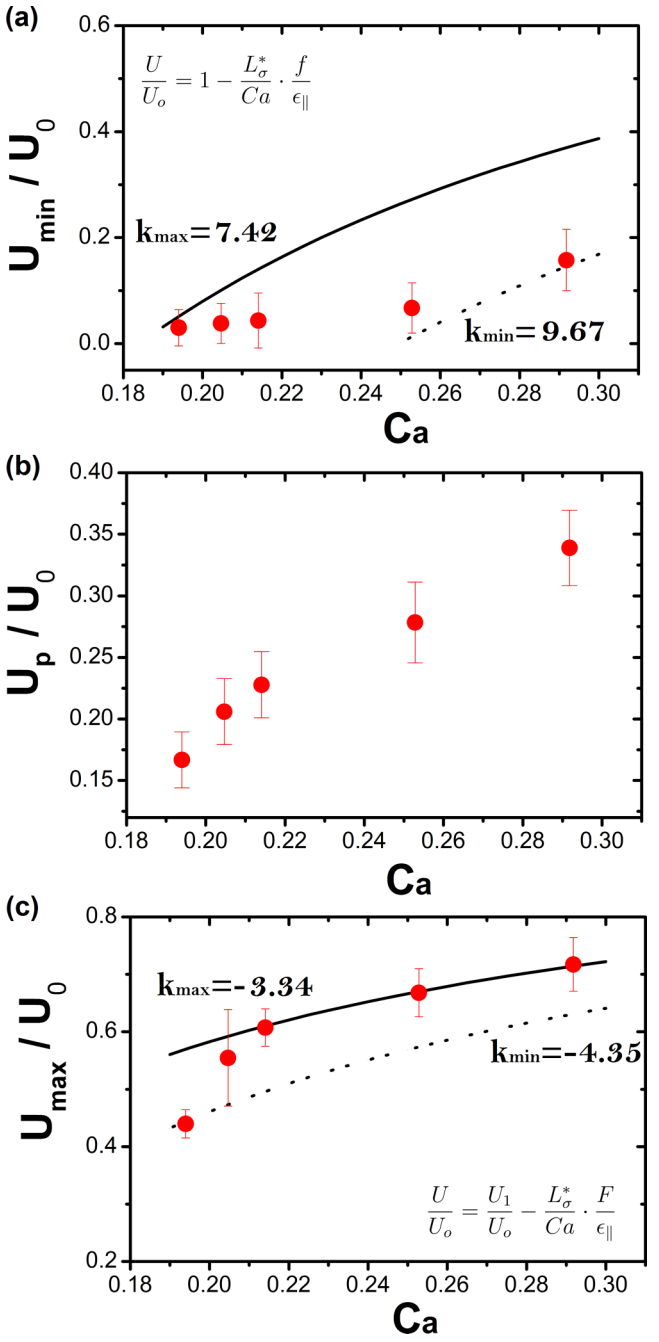

FIG. 5. (a) The minimum speed U_{min}/U_0 as a function of C_a during penetration. (b) The piercing speed U_{imp}/U_0, after meniscus rupture. (c) The maximum speed U_{max}/U_0 during penetration. The solid and the dashed lines show the predictions from Eq. (14) in panel (a) or Eq. (15) in panel (c), considering the maximum and the minimum value of the radius of dimensionless curvature of the meniscus, κ [Eq. (16)], respectively. Each point on the graph is the average of five measurements.

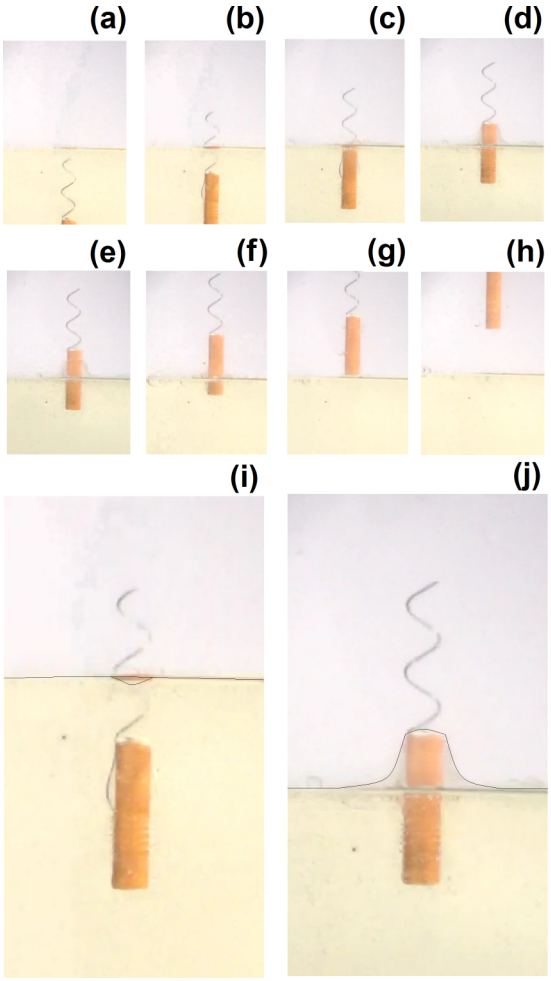

FIG. 6. Time sequence of the swimmer crossing the interface. (a)–(h) depict different relevant instants of the process, described in the text. Panels (i) and (j) are close-ups of the formation of the lower and upper meniscus, respectively. The inverse meniscus is formed under the small orange region close to the tail. A thin line was drawn at the interface location for clarity. The swimming speed for this case was 5.77 mm/s, which corresponds to a $\mathrm{Re} = 9.0 \times 10^{-3}$ and $\mathrm{Ca} = 0.27$.

B. Tail-first interaction

We found that the penetration process of the swimmer is significantly different when the tail interacts first with the interface. For the case of swimming in a homogeneous fluid, without the interface, the speed of swimming is practically the same regardless of the orientation of the tail/head, as shown in Fig. 2.

Figure 6 shows an image sequence of the penetration of the swimmer of when it moves tail-first, at different instants during the interaction with the interface. The complete dynamic of the helical swimmer is shown in Movie V2 (see Supplemental Material [49]). The velocity of the swimmer as a function of the position is shown in Fig. 7, for the corresponding images. Note that the position is that of the head with respect to the interface. Initially, the swimmer displaces vertically at a constant speed, U_o, Fig. 6(a), relatively far from the interface. When the head is at a distance of around 1.2 L_h from the interface, the swimmer velocity increases above its free value ($U > U_o$);

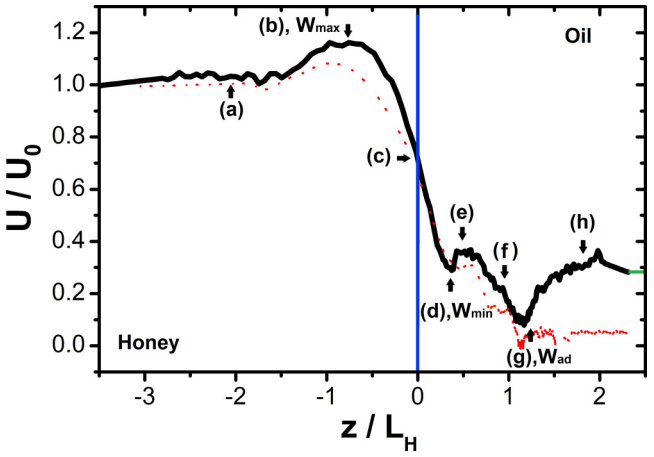

FIG. 7. Normalized speed of the swimmer U/U_0 as a function of position, z/D_h. The blue line indicates the location of the interface. The letters correspond to the time instants depicted in Fig. 6. The black and red curves correspond to swimmer speeds $U_o = 5.77$ mm/s and $U_o = 4.85$ mm/s, respectively. The green line (lower right side) indicates the dimensionless swimming speed in oil (single phase).

during this period, shown in Fig. 6(b), the tail is already interacting with the interface, generating a meniscus and the swimming speed reaches a maximum value, $W_{\max}$. Afterwards, as the head of the swimmer approaches the interface, the speed decreases, as shown in Fig. 6(c). The speed of the swimmer continues to decrease, as a new meniscus forms (of opposite curvature as that during the interaction of the tail). A local minimum velocity, $W_{\min}$ is observed at this instant, Fig. 6(d). As the process advances, the interface pierces, and the swimmer speed increases slightly, Fig. 6(e), to then decrease again as the meniscus recedes, Fig. 6(f). Once the head has completely passed the interface, a new smaller meniscus forms from the edge of the head causing the swimming speed to slow down, even more, Fig. 6(g), reaching its minimum value during the process, W_{ad}. At this point, the head appears to adhere to the interface. After that, when the head detaches completely from the interface, the swimmer accelerates until reaching the new swimming velocity U_1, Fig. 6(h). The process is also shown in terms of the swimming speed as a function of head-position in Fig. 7. The dynamic of the meniscus can be observed in Movie M2 (see Supplemental Material [49]).

In Fig. 7, the red-dashed curve shows the result of an experiment conducted at a smaller speed. As in the previous case, the evolution of the swimmer speed is the same for all speeds, but the different characteristic speeds are scaled down with the speed U_o. It is also noteworthy that for $\text{Ca} < 0.18$ (the same value as in the head-first case), the swimmer is not capable of penetrating the interface. In this case, the tail does pass through the interface but the head is not capable to pierce through the interface, and the swimmer stays rotating at the interface indefinitely.

A direct comparison between Figs. 4 and 7 clearly shows that the process of penetration is very different in the two cases; however, some features are similar in both cases. The first noticeable difference is the fact that in the head-first case, the swimmer speed is below the free swimming speed in the bottom fluid, $U/U_o < 1$, throughout the entire process. Conversely, for the tail-first case, there is a period during which $U/U_o > 1$. This increase in velocity occurs when the helix interacts with the interface, and an "inverted" meniscus is formed, as shown in Fig. 6(i). Interestingly, for the head-first case, the speed $U_{\max}$ is also reached when the helix is interacting with the interface. During this phase, the inverted meniscus is also observed as seen in Fig. 3(j). In both processes, when a 'regular' meniscus is formed around the head, as shown in Figs. 3(i) and 6(j), the speed of the swimmer is small. Also, in both cases, when the interface is pierced, there is a sudden increase in velocity until it reaches a maximum value in the position (d) and (e) in Figs. 4 and 7, respectively.

Only for tail-first case, the swimmer "adheres" to the interface before being able to completely cross, shown as position (g) in Fig. 7.

As in the previous case, the characteristic speeds can be determined for the range of Ca tested to characterize the process. In Fig. 8 the maximum speed, $W_{\max}$, the minimum speed, $W_{\min}$ and the speed during the interface adhesion, W_{ad} (all normalized) are shown as a function of the capillary number. All three characteristic speeds increase with Ca.

IV. MODELLING THE EFFECT OF THE INTERFACE ON THE MOTION OF THE SWIMMER

As shown above, when the swimmer crosses the interface, its velocity decreases due to the interfacial tension. Since during the process the interface is deformed to different degrees, the decrease of velocity depends on the crossing stage. Since the process occurs in a creeping flow regime, we can argue that the instantaneous speed of the swimmer is the result of a steady force balance. We can, therefore, write

$$F_p = F_d + F_b + F_\sigma, \tag{3}$$

where F_p is the propulsion force due to the rotation of the helical tail, F_d is the drag on the tail and head of the swimmer, F_b is the net buoyancy force, and F_σ is the force exerted on the swimmer by the deformed interface.

From the classical resistive force theory [20], we know that the propulsive force generated by the tail is

$$F_p \approx (\epsilon_\perp - \epsilon_\parallel)\mu\Omega R L_t \sin\theta \tag{4}$$

and that the drag force on the head and helix is

$$F_d \approx \frac{(\epsilon_\perp \sin^2\theta + \epsilon_\parallel \cos^2\theta)}{\cos\theta}\mu L_t U + \epsilon_0 \mu L_h U, \tag{5}$$

where $\epsilon_\perp$ and $\epsilon_\parallel$ are the normal and tangential drag coefficients, Ω is the rotational speed, R, L_t and θ are the dimensions of the helix (see Fig. 1), and μ is the fluid viscosity. The head is characterized by its length L_h and drag coefficient, ϵ_h. Neglecting the buoyancy force, and far from the interface, the swimming speed is

$$U_o = \Omega R(\xi - 1) f \sin\theta, \tag{6}$$

where f is defined as

$$f = \frac{\cos\theta}{1 + (\xi - 1)\sin^2\theta + \xi_0 L_h^* \cos\theta}, \tag{7}$$

where $L_h^* = L_h/L_t$, $\xi_0 = \epsilon_h/\epsilon_\parallel$, and $\xi = \epsilon_\perp/\epsilon_\parallel$.

The buoyancy force can be calculated as

$$F_b = \Delta\rho V g, \tag{8}$$

where $\Delta\rho = \rho_{\text{swimmer}} - \rho$ is the density difference between the swimmer and the fluid. V is the volume of the swimmer and g is the gravitational acceleration. If the $|\Delta\rho| \neq 0$, then the swimmer will either sink or ascend in the fluid. If this is the case, without rotation, then the sedimentation velocity of the swimmer would be

$$U_b = \frac{\Delta\rho V g}{\mu L_t \epsilon_\parallel} f. \tag{9}$$

This velocity is determined experimentally, as shown above, for both fluids, U_{b0} and U_{b1}.

The force due to interfacial tension can be obtained by simply considering

$$F_\sigma = \sigma_I L_\sigma, \tag{10}$$

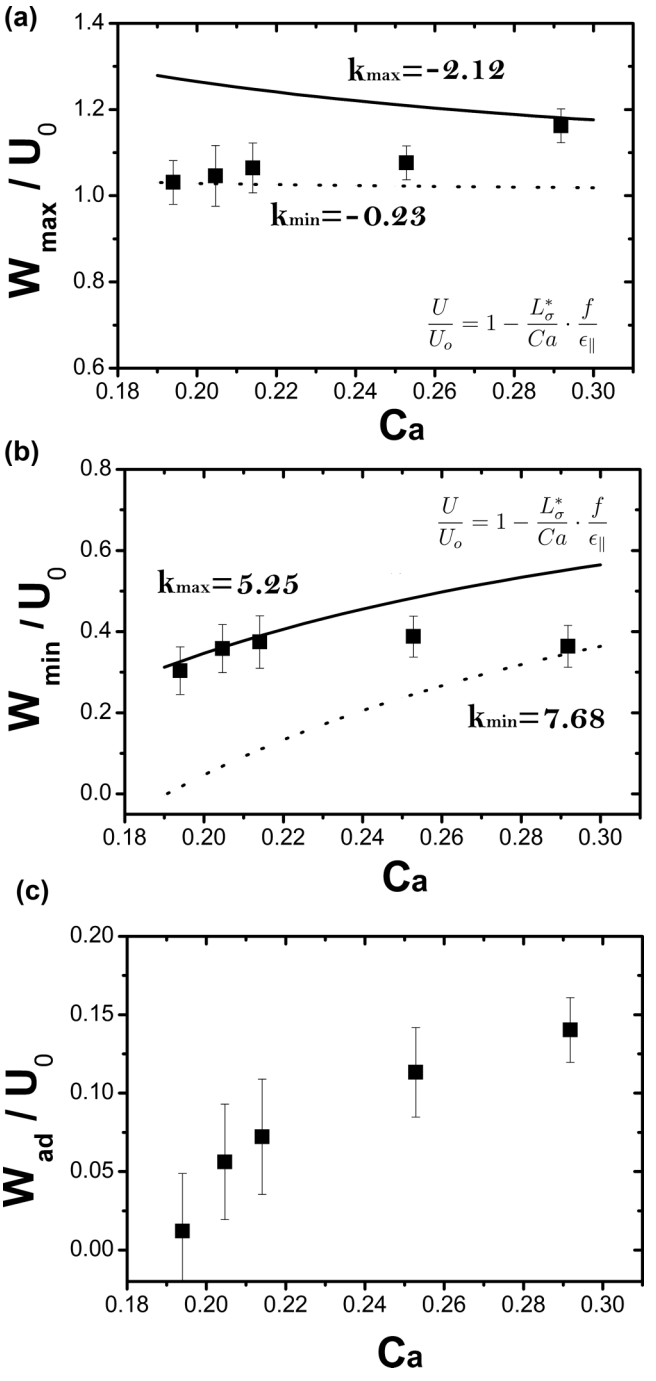

FIG. 8. (a) The maximum speed W_{max}/U_0 (b) the minimum W_{min}/U_0 and (c) the adhesion speed W_{ad}/U_0 during the penetration as a function of the capillary number, Ca. The solid and the dashed line show the predictions from Eq. (14), considering the maximum and the minimum value of the normalized radius of curvature of the meniscus, κ [Eq. (16)], respectively. Each point on the graph is the average of five measurements.

where L_σ is the radius of curvature of the deformed interface. A characteristic velocity scale can be obtained by balancing the interfacial and drag force to lead to

$$U_\sigma = \frac{\sigma_I L_\sigma}{\mu L_t \epsilon_\parallel} f. \tag{11}$$

Therefore, considering all forces we have

$$U = U_o - U_b - U_\sigma. \tag{12}$$

Note that when there is no interface, the speed of the swimmer is

$$U = U_o - U_b. \tag{13}$$

If the swimmer is in the bottom or top fluid, then $U = U_o$ or $U = U_1$, respectively. Both U_o and U_1 are determined experimentally.

Coming back to the case of interest, when the interface is present we can write Eq. (12) as

$$\frac{U}{U_o} = 1 - \frac{L_\sigma^*}{\mathrm{Ca}} \frac{f}{\epsilon_\parallel}, \tag{14}$$

where $L^* = L_h/L_t$ and $L_\sigma^* = L_\sigma/L_t$. This equation is applicable when the swimmer is immersed in the bottom fluid. However, when the swimmer is, mostly, in the top fluid, Eq. (12) can be written instead as

$$\frac{U}{U_o} = \frac{U_1}{U_o} - \frac{L_\sigma^*}{\mathrm{Ca}} \frac{f}{\epsilon_\parallel}. \tag{15}$$

Equations (14) and (15) can be used calculate the speed of the swimmer at different instants during the penetration process since most parameters are known (U_1/U_o, L^*, ξ, ξ_o, θ, $\epsilon_\parallel$) for a given value of Ca. Note that for small θ, f is reduced to

$$f = \frac{2}{1 + \xi_o L_h^*}$$

The values of the drag coefficients, $\epsilon_\parallel$, ϵ_h, and $\epsilon_\perp$ can be obtained from Ref. [50], resulting in: $\epsilon_h = 1.632\pi$, $\epsilon_\parallel = 0.753\pi$ and $\epsilon_\perp = 1.093\pi$ for which $\xi = 1.45$ and $\xi_0 = 2.167$. From the geometry of the swimmer used in this study $L^* = 1$, as shown in Fig. 1. The only unknown parameter is L_σ^*, which is the ratio of the radius of curvature of the deformed interface to the length of the tail. From the images in Figs. 4 and 6 we can argue that the curvature of the interface is proportional to the diameter of the head; therefore, we can define a normalized meniscus curvature as

$$\kappa = \frac{L_\sigma}{D_h}. \tag{16}$$

From this definition, we can write $L_\sigma^* = \kappa D_h/L_t$. For the swimmer used in the study, $L_t/D_h = 5.33$. Hence, κ is the only unknown parameter, which we can be easily fit to the data.

It is important to note that although the model does account for different amounts of buoyancy in each fluid [Eqs. (14) and (15)], it does not consider the effect of a gradient of buoyancy. While the volume of the helix may be negligible, the change in buoyancy force when the head is moving across the interface may be important because the swimmer does not have a uniform density. The volume of the helix is indeed smaller that the head but the helix is denser, as described in Sec. II. We expect the buoyancy gradient effect to be small but the model does not account for it.

A. Comparison with the experiments

From the process of crossing the interface, shown in Figs. 4 and 7, two characteristic speeds can be calculated considering the model presented above. These calculations can be directly contrasted with the experimental measurements shown in Figs. 5 and 8.

TABLE II. Parameters for the theoretical predictions. The maximum and the minimum value of the normalized radius of curvature of the meniscus, κ [Eq. (16)], for the characteristic speeds.

	$U_{\max}$	$U_{\min}$	$W_{\max}$	$W_{\min}$
$\kappa_{\max}$	−3.34	7.42	−2.12	5.25
$\kappa_{\min}$	−4.35	9.67	−0.23	7.68

We begin considering the value of $U_{\min}$ during the head-first interaction. This value of the swimmer speed is observed when the head is interaction with the interface and a meniscus forms and it is attached to the head, as shown in Fig. 3(i). Since the swimmer is mostly immersed in the bottom fluid, we should consider Eq. (14). The lines in Fig. 5(a) show the predictions, considering two values of κ. This parameter measures how large is the radius of curvature of the meniscus with respect to the diameter of the head. The values of κ used to fit the data, shown in Table II, ranged from 6.8 to 9.2, which are in reasonable agreement to what is shown in the image. In other words, when the meniscus forms around the head, it has a large radius or curvature, which acts to reduce the swimming speed. The data and the prediction match reasonably well, indicating that $U_{\min}/U_o$ increases with Ca. The fact that the data does not match to a single line indicates that the curvature of the meniscus changes with the value of Ca, which is expected. For the case of $U_{\max}$, which occurs when the helix is interacting with the interface as seen in Fig. 3(j), the head of the swimmer is in the upper fluids; therefore, Eq. (15) should be considered. Interestingly, in this case the curvature of the interfaces is opposite to the previous case: it is formed into the bottom fluid. Therefore, the force induced by the interface acts in the direction of motion, enhancing the swimmer speed. To match the experimental values of $U_{\max}$, the values of κ ranged from -2.0 to -1.1 in good agreement with the visual information from the images. The predictions of Eq. (15) are shown in Fig. 5(c). Again, no single curve can be matched to all the measurements because the shape of the meniscus most likely changes with Ca but the trend is consistent with the data. As the Ca value increases, so does the value of $U_{\max}/U_o$.

For the tail-first interaction, we can predict the values of $W_{\max}$ and $W_{\min}$. For $W_{\max}$, the swimmer is mostly immersed in the bottom fluid then, we consider Eq. (14) but in this case, the helical tail is interaction with the interface, as shown in Fig. 6(i). As in the previous case, an inverted meniscus is formed; hence, the interfacial tension force pushes the swimmer forward leading to speed with is, in fact, $U/U_o > 1$ (faster than the free swimming speed). For this case, the values of κ used to match the result ranged from -1.9 to -0.2, in agreement to what it is observed in the images. The predictions are shown along with the data in Fig. 8(a). Note that the data shows a weak dependence of $W_{\max}/U_o$ with Ca and that in this case, the prediction shows that the maximum speed decreases with Ca. Again, the disagreement most likely results from the values of the curvature that depend on Ca itself. Finally, we can predict the value of the speed when the head is crossing the interface, with the meniscus still attached to the head, as shown in Fig. 6(j). This speed is referred to as $W_{\min}$. For this instant, since the head is in the middle of the interface, we can still use Eq. (14) for which the interfacial force acts in the direction opposite to the swimmer motion, slowing it down. During this phase, the radius of curvature is large; the values of κ used for the fitting shown in Fig. 8(b) range from 4.8 to 7.0. As in the previous cases, the experimental trend is captured by the model: $W_{\min}/U_o \sim \mathrm{Ca}$.

The simple steady model appears to capture the experimental measurements reasonably well. A detailed measurement, or modeling, of the shape of the interface for the head or tail interactions, would be needed to improve the model. As presented here, the model is aimed at capturing the main features of the crossing process.

V. CONCLUSIONS

In this investigation, experiments were conducted with synthetic magnetic helical swimmers to study the dynamics of crossing across the interface between two immiscible fluids. The interfacial

tension plays a significant role in the dynamics of the penetration of a self-propelled swimmer. The dynamics of the process are complex due to the continuous deformation of the interface. Interestingly, the interface either slows down or hastens the speed of the swimmer. When the head of the swimmer interacts with the interface, a convex meniscus appears which induces a force in an opposite direction of the motion, reducing the speed. Conversely, we the helical tail interacts with the interface, the meniscus is concave (opposite curvature) which induces a force on the swimmer in the direction of motion, increasing the speed. Due to these different effects, the process of penetration is significantly different if the swimmer reaches the interface head-first or tail-first. This system is aimed to emulate the process through which bacteria are capable of penetrating mucus layers or membranes to cause infections. The mechanical description of these processes has not been explored in depth to date. Even in this simplified situation, the process exhibits rich dynamics. Our study could serve as a first step to characterize the dynamics of the process. We envision extending the scope to other swimming strategies, used by other microorganisms, and considering layers of variable viscosity as those found in the digestive system.

ACKNOWLEDGMENT

J.G.G. acknowledges financial support from the DGAPA-UNAM posdoctoral program.

[1] J. M. Martinko and M. T. Madigan, *Brock Biology of Microorganisms* (Pearson, London, UK, 2005).
[2] E. A. Gaffney, H. Gadêlha, D. J. Smith, J. R. Blake, and J. C. Kirkman-Brown, Mammalian sperm motility: Observation and theory, Annu. Rev. Fluid Mech. **43**, 501 (2011).
[3] S. Vogel, *Life in Moving Fluids: The Physical Biology of Flow* (Princeton University Press, Princeton, NJ, 1996).
[4] K. F. Jarrell and M. J. McBride, The surprisingly diverse ways that prokaryotes move, Nature Rev. Microbiol. **6**, 466 (2008).
[5] D. B. Kearns, A field guide to bacterial swarming motility, Nature Rev. Microbiol. **8**, 634 (2010).
[6] R. J. Lee, G. Xiong, J. M. Kofonow, B. Chen, A. Lysenko, P. Jiang, V. Abraham, L. Doghramji, N. D. Adappa, J. N. Palmer *et al.*, T2r38 taste receptor polymorphisms underlie susceptibility to upper respiratory infection, J. Clin. Invest. **122**, 4145 (2012).
[7] S. C. Kinnamon, Taste receptor signaling—From tongues to lungs, Acta Physiol. **204**, 158 (2012).
[8] S. L. Gorbach, Microbiology of the gastrointestinal tract, *Medical Microbiology*, 4th ed. (University of Texas, Medical Branch at Galveston, 1996).
[9] I. Brook, Microbiology and management of abdominal infections, Dig. Dis. Sci. **53**, 2585 (2008).
[10] F. S. Oluwole, *Helicobacter pylori*: A pathogenic threat to the gastric mucosal barrier, Afr. J. Med. Med. Sci. **44**, 289 (2015).
[11] H. Choi, J. Choi, J. Seo, B. Kim, M. Rho, J. K. Han, and J. G. Kim, *Helicobacter pylori*-derived extracellular vesicles increased in the gastric juices of gastric adenocarcinoma patients and induced inflammation mainly via specific targeting of gastric epithelial cells, Exp. Mol. Med. **49**, e330 (2017).
[12] J. G. Kusters, A. HM van Vliet, and E. J. Kuipers, Pathogenesis of *Helicobacter pylori* infection, Clin. Microbiol. Rev. **19**, 449 (2006).
[13] D. Bray, *Cell Movements: From Molecules to Motility* (Garland Science, New York, NY, 2000).
[14] V. de Lorenzo, Blueprint of an oil-eating bacterium, Nature Biotech. **24**, 952 (2006).
[15] K. Zhang, Y. Sun, Z. Cui, D. Yu, L. Zheng, P. Liu, and Z. Lv, Periodically spilled-oil input as a trigger to stimulate the development of hydrocarbon-degrading consortia in a beach ecosystem, Sci. Rep. **7**, 12446 (2017).
[16] A. B. Al-Hawash, M. A. Dragh, S. Li, A. Alhujaily, H. A. Abbood, X. Zhang, and F. Ma, Principles of microbial degradation of petroleum hydrocarbons in the environment, Egypt. J. Aquat. Res. **44**, 71 (2018).

[17] E. Lauga, Bacterial hydrodynamics, Annu. Rev. Fluid Mech. **48**, 105 (2016).
[18] E. Lauga and T. R. Powers, The hydrodynamics of swimming microorganisms, Rep. Prog. Phys. **72**, 096601 (2009).
[19] J. Gray and G. J. Hancock, The propulsion of sea-urchin spermatozoa, J. Exp. Biol. **32**, 802 (1955).
[20] J. Lighthill, Flagellar hydrodynamics, SIAM Rev. **18**, 161 (1976).
[21] L. Zhang, J. J. Abbott, L. Dong, B. E. Kratochvil, D. Bell, and B. J. Nelson, Artificial bacterial flagella: Fabrication and magnetic control, App. Phys. Lett. **94**, 064107 (2009).
[22] H. C. Berg, *E. Coli in Motion* (Springer, Berlin, 2004).
[23] E. G. Richardson, The impact of a solid on a liquid surface, Proc. Phys. Soc. **61**, 352 (1948).
[24] H. C. Maru, D. T. Wasan, and R. C. Kintner, Behavior of a rigid sphere at a liquid-liquid interface, Chem. Eng. Sci. **26**, 1615 (1971).
[25] A. S. Geller, S. H. Lee, and L. G. Leal, The creeping motion of a spherical particle normal to a deformable interface, J. Fluid Mech. **169**, 27 (1986).
[26] M. Lee, R. G. Longoria, and D. E. Wilson, Cavity dynamics in high-speed water entry, Phys. Fluids **9**, 540 (1997).
[27] V. Duclaux, F. Caille, C. Duez, C. Ybert, L. Bocquet, and C. Clanet, Dynamics of transient cavities, J. Fluid Mech. **591**, 1 (2007).
[28] H. Lhuissier, C. Sun, A. Prosperetti, and D. Lohse, Drop Fragmentation at Impact onto a Bath of an Immiscible Liquid, Phys. Rev. Lett. **110**, 264503 (2013).
[29] S. H. Tsai, J. S. Wexler, J. Wan, and H. A Stone, Microfluidic ultralow interfacial tensiometry with magnetic particles, Lab Chip **13**, 119 (2013).
[30] G. Birkhoff and E. H. Zarantonello, *Jets, Wakes, and Cavities* (Academic Press, San Diego, CA, 1957).
[31] T. T. Truscott, B. P. Epps, and J. Belden, Water entry of projectiles, Annu. Rev. Fluid Mech. **46**, 355 (2014).
[32] S. Hartland, The approach of a rigid sphere to a deformable liquid/liquid interface, J. Colloid Interface Sci. **26**, 383 (1968).
[33] S. Hartland, The profile of the draining film between a rigid sphere and a deformable fluid-liquid interface, Chem. Eng. Sci. **24**, 987 (1969).
[34] C. Darwin, Note on hydrodynamics, In *Mathematical Proceedings of the Cambridge Philosophical Society*, Vol. 49 (Cambridge University Press, Cambridge, UK, 1953), pp. 342–354.
[35] I. R. Peters, M. Madonia, D. Lohse, and D. van der Meer, Volume entrained in the wake of a disk intruding into an oil-water interface, Phys. Rev. Fluids **1**, 033901 (2016).
[36] J. W. J. De Folter, V. W. A. De Villeneuve, D. G. A. L. Aarts, and H. N. W. Lekkerkerker, Rigid sphere transport through a colloidal gas-liquid interface, New J. Phys. **12**, 023013 (2010).
[37] N. Dietrich, S. Poncin, and H. Z. Li, Dynamical deformation of a flat liquid–liquid interface, Exp. Fluids **50**, 1293 (2011).
[38] J.-L. Pierson and J. Magnaudet, Inertial settling of a sphere through an interface. Part 1. From sphere flotation to wake fragmentation, J. Fluid Mech. **835**, 762 (2018).
[39] J.-L. Pierson and J. Magnaudet, Inertial settling of a sphere through an interface. Part 2. Sphere and tail dynamics, J. Fluid Mech. **835**, 808 (2018).
[40] S. Liang, J. Li, H. Chen, and Q. Xu, Film coating on a small sphere crossing an oil-water interface, Phys. Rev. Fluids **3**, 124003 (2018).
[41] F. A. Godínez, L. Koens aand T. D. Montenegro-Johnson, R. Zenit, and E. Lauga, Complex fluids affect low-Reynolds number locomotion in a kinematic-dependent manner, Exp. Fluids **56**, 97 (2015).
[42] S. Gomez, F. Godinez, E. Lauga, and R. Zenit, Helical propulsion in shear-thinning fluids, J. Fluid Mech. **812**, R3 (2016).
[43] F. A. Godínez, O. Chávez, and R. Zenit, Note: Design of a novel rotating magnetic field device, Rev. Sci. Instrum. **83**, 066109 (2012).
[44] M. Hoorfar, M. A. Kurz, Z. Policova, M. L. Hair, and A. W. Neumann, Do polysaccharides such as dextran and their monomers really increase the surface tension of water? Langmuir **22**, 52 (2006).
[45] J. Peukes and T. Betz, Direct measurement of the cortical tension during the growth of membrane blebs, Biophys J. **107**, 1810 (2014).

[46] M. J. Pelczar, R. D. Reid, and E. C. Sun Chan, *Microbiology* (McGraw Hill, New York, 1977).
[47] A. Swidsinski, B. C. Sydora, Y. Doerffel, V. Loening-Baucke, M. Vaneechoutte, M. Lupicki, J. Scholze, H. Lochs, and L. A. Dieleman, Viscosity gradient within the mucus layer determines the mucosal barrier function and the spatial organization of the intestinal microbiota, Inflamm. Bowel Dis. **13**, 963 (2007).
[48] E. Fernandez, D. Lopez, C. Mijangos, M. Duskova-Smrckova, M. Ilavsky, and K. Dusek, Rheological and thermal properties of agarose aqueous solutions and hydrogels, J. Polymer Sci. B **46**, 322 (2008).
[49] See Supplemental Material at http://link.aps.org/supplemental/10.1103/PhysRevFluids.4.083102 for supplementary movies.
[50] J. Gray, The movement of sea-urchin spermatozoa, J. Exp. Biol. **32**, 775 (1955).